Earth, Planets and Space

FULL PAPER Open Access

Semi-analytical solutions of seismo-electromagnetic signals arising from the motional induction in 3-D multi-layered media: part II—numerical investigations

Hengxin Ren[1,2*], Ling Zeng[2], Yao-Chong Sun[2], Ken'ichi Yamazaki[3], Qinghua Huang[4] and Xiaofei Chen[2,5]

Abstract

In this paper, numerical computations are carried out to investigate the seismo-electromagnetic signals arising from the motional induction effect due to an earthquake source embedded in 3-D multi-layered media. First, our numerical computation approach that combines discrete wavenumber method, peak-trough averaging method, and point source stacking method is introduced in detail. The peak-trough averaging method helps overcome the slow convergence problem, which occurs when the source–receiver depth difference is small, allowing us to consider any focus depth. The point source stacking method is used to deal with a finite fault. Later, an excellent agreement between our method and the curvilinear grid finite-difference method for the seismic wave solutions is found, which to a certain degree verifies the validity of our method. Thereafter, numerical computation results of an air–solid two-layer model show that both a receiver below and another one above the ground surface will record electromagnetic (EM) signals showing up at the same time as seismic waves, that is, the so-called coseismic EM signals. These results suggest that the in-air coseismic magnetic signals reported previously, which were recorded by induction coils hung on trees, can be explained by the motional induction effect or maybe other seismo-electromagnetic coupling mechanisms. Further investigations of wave-field snapshots and theoretical analysis suggest that the seismic-to-EM conversion caused by the motional induction effect will give birth to evanescent EM waves when seismic waves arrive at an interface with an incident angle greater than the critical angle $\theta_c = \arcsin(V_{sei}/V_{em})$, where V_{sei} and V_{em} are seismic wave velocity and EM wave velocity, respectively. The computed EM signals in air are found to have an excellent agreement with the theoretically predicted amplitude decay characteristic for a single frequency and single wavenumber. The evanescent EM waves originating from a subsurface interface of conductivity contrast will contribute to the coseismic EM signals. Thus, the conductivity at depth will affect the coseismic EM signals recorded nearby the ground surface. Finally, a fault rupture spreading to the ground surface, an unexamined case in previous numerical computations of seismo-electromagnetic signals, is considered. The computation results once again indicate the motional induction effect can contribute to the coseismic EM signals.

*Correspondence: renhx@sustech.edu.cn
[1] Shenzhen Key Laboratory of Deep Offshore Oil and Gas Exploration Technology, Southern University of Science and Technology, Shenzhen 518055, Guangdong, China
Full list of author information is available at the end of the article

Keywords: Seismo-electromagnetic signals, Motional induction effect, Numerical computation, Coseismic EM signals, Evanescent EM waves

Introduction

In the companion paper (Sun et al. 2021), which is part I of current work, a set of systematic semi-analytical solutions of the seismo-electromagnetic signals arising from the motional induction in 3-D multi-layered media due to an earthquake source was obtained. In addition to the seismic and electromagnetic (EM) signals in the solid, EM signals in the air can also be calculated by the derived semi-analytical solutions. In the derivation process, Sun et al. (2021) utilized the linear superposition principle, applied the analytical regularization approach (Chen 1999; Ren et al. 2010a) by introducing two artificial interfaces infinitely close to the source, and adopted the Luco–Apsel–Chen (LAC) generalized reflection and transmission (GRT) method (Luco and Apsel 1983; Chen 1993, 1999; Ren et al. 2007, 2010b, 2012, 2016a, 2016b, 2020). These measures bring higher efficiency and stability to the numerical computation of the semi-analytical solutions.

Although the motional induction effect has been proposed as a possible generation mechanism of seismo-electromagnetic phenomena since nearly three decades ago (Gershenzon et al. 1993), quantitative investigations on this topic are very few. To our knowledge, only two works (Yamazaki 2012; Gao et al. 2019) provide solutions and conduct computations for seismo-electromagnetic signals arising from motional induction effect in multi-layered media. Considering a simple situation in which seismic waves are approximated by plane waves and the electrical conductivity of the Earth's crust has a stratified structure, Yamazaki (2012) derived analytical solutions of the EM responses and conducted numerical analysis. The numerical computations of Yamazaki (2012) aimed at some given periods (or frequencies) of seismic waves and did not require wavenumber integration. It should be noted that the solutions of Yamazaki (2012) are only applicable in the far-field condition because of the applied approximation of seismic plane waves. Considering 2-D case, Gao et al. (2019) used the global matrix method to derive the solutions of seismo-electromagnetic signals that are expressed as wavenumber integrations. They computed these wavenumber integrations to achieve the space-domain solutions. As shown by Eqs. (21) and (22) of Gao et al. (2019), 2-D solutions concerned in their work can be computed by inverse Fourier transform with respect to the wavenumber, because they applied a space-to-wavenumber Fourier transform to the involved wavefields. The 2-D solutions of Gao et al. (2019) are only applicable for a special case in which the fault plane is perpendicular to the wave propagation plane. For the 3-D case considered in this work, although the semi-analytical solutions (Sun et al. 2021) are also expressed as wavenumber integrations, they should be regarded as the summation of several inverse Hankel transforms (see Appendix A). Therefore, the 3-D semi-analytical solutions (Sun et al. 2021) cannot be computed by the inverse Fourier transform. Instead, they can be computed using the well-known discrete wavenumber method (Bouchon and Aki 1977; Bouchon 1981, 2003). It should be mentioned, for both 2-D and 3-D cases, a slow convergence problem will occur in the numerical computation of the solutions when the source and receiver are located at close or same depths. This slow convergence problem has not been solved in the work of Gao et al. (2019).

The discrete wavenumber method, which introduces an infinite set of secondary sources of concentric rings distributed at equal radial intervals L_p (spatial periodicity) to transform the wavenumber integration into summation (Bouchon and Aki 1977; Bouchon 1981, 2003), has been applied in the numerical modelling studies of electrokinetic effect (e.g., Haartsen and Pride 1997; Garambois and Dietrich 2002; Ren et al. 2012). In these numerical computations of seismo-electromagnetic signals induced by electrokinetic effect, it was found using largest seismic wave velocity to determine the spatial periodicity L_p is sufficient to guarantee the accuracy of numerical solutions. In this work, we also apply the discrete wavenumber method to numerically compute the semi-analytical solutions of Sun et al. (2021). We adopt the peak-trough averaging method (Zhang et al. 2001, 2003) to overcome the slow convergence problem. Besides, we utilize the point source stacking method (Olson and Apsel 1982; Ren et al. 2012) to deal with the case of a finite fault.

The remainder of this paper is organized as follows. First, we introduce our numerical computation approach enabling us to deal with any focus depth and to consider either a double couple point source or a finite fault. Second, we try to verify the proposed method by comparing with another numerical method for the seismic wave solutions. Last, we conduct numerical investigations that are different from those of Yamazaki (2012) and Gao et al. (2021). The coseismic characteristic of the EM signals, the generation of

evanescent EM waves on interfaces, and the effect of conductivity at depth on EM signals are presented and discussed.

Numerical computation approach

In the following context, we specify the detailed implementation of the discrete wavenumber method (Bouchon and Aki 1977; Bouchon 1981, 2003), the peak-trough averaging method (Zhang et al. 2001, 2003), and the point source stacking method (Olson and Apsel 1982; Ren et al. 2012) in our numerical computation of seismo-electromagnetic signals arising from the motional induction due to a double couple point source or a finite fault embedded in a 3-D multi-layered media.

Discrete wavenumber method

According to Bouchon and Aki (1977) and Bouchon (1981, 2003), the spatial periodicity of secondary sources L_p determines the wavenumber sampling Δk used in summation:

$$\Delta k = \frac{2\pi}{L_p}. \tag{1}$$

Considering a cylindrical coordinates system with a source located at (0, 0, z_s) and a receiver located at (r, θ, z), the spatial periodicity L_p should satisfy the condition that "pseudo" waves generated by the secondary sources do not enter the observational time window $t \in [0, t_{\max}]$, that is, there will be no interference from the nearest secondary source to the receiver's recording before the time of $t = t_{\max}$. This specific condition can be written as follows:

$$L_p > 2r, \quad \sqrt{(L_p - r)^2 + (z - z_s)^2} > v_{\max} t_{max} \tag{2}$$

where $v_{\max}$ should be, in principle, the maximum wave velocity in the medium. Consequently, when considering the propagation of coupled seismic and EM waves, the value of $v_{\max}$ theoretically should be the largest EM wave velocity, which implies a very large periodicity L_p. Thus, according to Eq. (1), we should use a very small wavenumber sampling Δk to ensure the correctness of the calculation results, which leads to unacceptably long computation time in practice. However, for the converted EM waves whose phase velocity is $1/\sqrt{\mu(\varepsilon + i\sigma/\omega)}$ (where μ is magnetic permeability; ε is electrical permittivity; σ is conductivity; ω is the circular frequency), we have numerically verified that the computed synthetic signals are identical whether $v_{\max}$ is based on the largest seismic or EM wave velocity. The reason is that, although secondary sources also give birth to converted EM waves that propagate in both air and solid with EM wave velocity of the media, those converted EM waves contributed from secondary sources show a rapid amplitude decrease as the offsets between secondary sources and receiver increase. A spatial periodicity L_p satisfying Eq. (2) with $v_{\max}$ based on the largest seismic wave velocity can guarantee that the secondary source–receiver offsets are long enough for the attenuation of the converted EM waves from secondary sources. As a result, the amplitudes of EM waves generated by secondary sources are always negligible with respect to the EM waves generated by the principal source. Such a measure of using largest seismic wave velocity as $v_{\max}$ to determine L_p has been adopted in some previous studies that numerically calculated seismo-electromagnetic signals induced by electrokinetic effect (e.g., Haartsen and Pride 1997; Garambois and Dietrich 2002; Ren et al. 2012).

To perform the summation of secondary sources, one needs to remove the singularities of the integrands from the real k-axis. This can be achieved by giving the real circular frequency ω_R a small imaginary part ω_I. Hence, we use a complex circular frequency:

$$\omega = \omega_R + i\omega_I, \text{ with } \omega_I > 0, \tag{3}$$

when a time dependence of $e^{-i\omega t}$ is considered. In this way, the singularities are located in the first and third quadrants of the complex k plane on the straight line passing through the origin, eliminating the singularities on the real k-axis (Aki and Richards 1980). The value of ω_I is usually chosen to be (Haartsen and Pride 1997):

$$\omega_I = \frac{\pi}{t_{max}}. \tag{4}$$

The introduction of complex frequencies leads to a smoothing effect on the spectrum, because it can relatively increase the strength of earlier-arriving signal. Besides, it can also reduce the interference generated from the nearest secondary source (Bouchon and Aki 1977). The influence of the imaginary part of the complex frequency can be removed from the final time-domain solutions using the inverse Fourier transformation with the kernel $\exp(-i\omega_R t + \omega_I t)$.

Peak-trough averaging method

According to Sun et al. (2021), the semi-analytical solutions of seismic waves or EM signals due to an arbitrary point seismic source buried in a multi-layered media can be expressed as a summation of the products of the

radiation patterns and the following type of oscillatory integrals:

$$I_n(r,z,z_s,\omega) = \int_0^{+\infty} S(k,z,z_s,\omega)\cdot J_n(\mathrm{kr})\mathrm{d}k, \tag{5}$$

where r is the epicentral distance; z is the receiving point depth; z_s indicates the source depth; k is the horizontal wavenumber; ω is the circular frequency; $J_n(kr)$ is the nth order Bessel function of the first kind; $S(k, z, z_s, \omega)$ represents the kernel function containing the attenuation factor. If the source–receiver depth difference becomes smaller, the attenuation factor contained in the kernel function will have weaker effect. Then, under the combined action of the kernel function and the Bessel function, the convergence of wavenumber integration becomes extremely slow. Thus, to obtain accurate computation results, one has to take a large upper limit of truncated integral, which leads to extremely low computation efficiency (Zhang et al. 2001, 2003).

The peak-trough averaging method (Zhang et al. 2001, 2003), which is mathematically simple and easy to implement in practice, has been proven an effective and efficient method to overcome this slow convergence problem. When the wavenumber is greater than a certain critical value, the integral value oscillates around a certain value as the integral upper limit increases, and its envelope is a monotonous and smooth attenuation curve, which is characterized by slow convergence. The peak-trough averaging method can utilize a small number of peak and trough values to achieve the purpose of efficient and high-precision computation. The reason is that the peak-trough distribution of the slow convergence integral also appears as a monotonically decayed alternating sequence. Therefore, the peak and trough values of the integration curve can be extracted to form a slow-convergent sequence, whose convergence value (i.e., the integral value when the upper limit of the integral tends to infinity) can be obtained quickly and accurately using the repeated average method (Dahlquist and Björck 1974). The specific process of the peak-trough averaging method can be divided into the following 3 steps:

Determine the critical wave value k_c

When $k > k_c$, the envelope of the integral value appears as a monotonic attenuation curve, so we first determine the critical wave value k_c, which can be given by the following empirical formula:

$$k_c = \alpha\sqrt{(\omega_R^2+\omega_I^2)}\Big/ v_{\min}, \tag{6}$$

where v_{min} is the minimum velocity of the structure model; ω_R is the real circular frequency; ω_I is the imaginary circular frequency; α is an empirical coefficient, which is sufficiently large to ensure the decaying property of the integral at $k > k_c$. As suggested by Zhang et al. (2001, 2003), we use an empirical coefficient of 1.5 in our numerical computations.

Determine the peak and trough values

When $k > k_c$, we first need to determine the initial peaks and troughs. Therefore, we record the positions of each adjacent three integral sampling points k_i and corresponding function values (k_i, G_i) ($i = 1, 2, 3$). If G_2 is greater or smaller than G_1 and G_3, then (k_2,G_2) is an initial position of a peak or trough. If not, it proves that there is no peak or trough in this interval. In either case, move one point forward to form a new group of three successive integration sampling points and corresponding function values, and then repeat the above process, continuously increasing the wave number k by a fixed step Δk, which is specified by Eq. (1), until enough peaks and troughs are obtained.

The accuracy of the peak-trough averaging method depends on the accuracy of the function values of the peaks and troughs. However, due to the limitation of the step size, the accuracy of the initial peaks and troughs determined through the above screening process is often not accurate enough and must be further improved. Zhang et al. (2001, 2003) proposed using the quadratic interpolation technique to find the accurate peaks and troughs within the allowable range of computation error. According to the above steps, enough initially determined peaks or troughs positions (k_2, G_2) with their adjacent points (k_1, G_1) and (k_3, G_3) have been recorded. Although the location of the peak or trough is rough, it can be judged that the accurate peak or trough is located in the (k_1, k_3) interval. Thus, the following quadratic interpolation polynomial can be constructed:

$$G(k) = a\left(\frac{k-k_1}{k_3-k_1}\right)^2 + b\left(\frac{k-k_1}{k_3-k_1}\right) + c, \tag{7}$$

where $a = 2G_3 - 4G_2 + 2G_1$, $b = 4G_2 - G_3 - 3G_1$ and $c = G_1$. The exact coordinates of the peak ($a < 0$) or trough ($a > 0$) is $\left(k_1 - \frac{b}{2a}(k_3 - k_1), G_1 - \frac{b^2}{4a}\right)$. Using the above method, a series of accurate peaks and troughs can be obtained.

Determine the integral convergence value

After finding a series of accurate peaks and troughs, and composing them into an oscillating slow convergence sequence, one can use the repeated average method

(Dahlquist and Björck 1974) to obtain the convergence value, i.e., the required integral value.

The point source stacking method

It is known that, a fault can be considered as a double couple point source under the far-field condition. However, under near-field condition, a finite fault must be considered as a non-point source, because the point-source approximation in this case will result in unacceptable errors of the wavefields computed (Ren et al. 2012). It is usually difficult to directly calculate the field generated by a finite fault. One solution to this problem is the point source stacking method (Olson and Apsel 1982; Ren et al. 2012).

For a finite fault, the generated seismic or EM wavefields at one spatial point are the integral of Green's function over the area of the finite fault. In the numerical computation, integral is carried out by summation. Therefore, the finite fault can be discretized into a lot of cells. Each can be approximately treated as a point source located at the cell center when its area is sufficiently small. In this way, the finite fault can be represented by the serried distribution of numerous point sources in the fault area. Thus, the seismic or EM wavefields at one spatial point are the stacking of wavefields generated by each point source, which can be numerically computed through the semi-analytical solutions derived by Sun et al. (2021).

In theory, smaller cell size leads to more accurate numerical solutions. However, in actual numerical calculations, smaller cell size also means longer the calculation time. Therefore, we need to select a suitable cell size, which can not only reduce the computation time as much as possible but also satisfy the required precision. This aim can be achieved by the following steps (which take seismic wave solutions as an example): (i) Given a discretization scheme, for instance, $\Delta s = (L/M)(W/N)$ (where L and W indicate the length and width of the finite fault; M and N are positive integers; Δs is the cell area), we compute the seismic wave solutions $\mathbf{u}_{(1)}$ for the receiver point; (ii) Double the positive integers ($2M \rightarrow M$ and $2N \rightarrow N$) and recompute the seismic wave solutions $\mathbf{u}_{(2)}$; (iii) Calculate the residual error e_{res} through the following formula:

$$e_{\mathrm{res}} = \sqrt{\sum_i \left|\mathbf{u}_{(2)}(t_i) - \mathbf{u}_{(1)}(t_i)\right|^2} \Big/ \sqrt{\sum_i \left|\mathbf{u}_{(1)}(t_i)\right|^2}; \tag{8}$$

(iv) Compare the residual error e_{res} with the required precision p_{req}. If $e_{\mathrm{res}} < p_{\mathrm{req}}$, the used cell size will be considered suitable and the computation results will be taken as the correct solutions. Otherwise, repeat the steps (ii)–(iv) until the correct solutions are obtained. The above steps should also be applied to the solutions of EM fields. A required precision of $p_{\mathrm{req}} = 10^{-6}$ is adopted in this study.

In the following numerical computation, the North, East and downward directions are set to be x-, y- and z-directions, respectively.

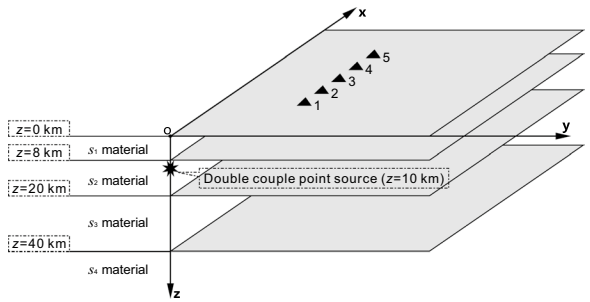

Fig. 1 Configuration of a four-layer model used for verifying the validity of the seismic waves computed by the proposed method. Five receivers marked as 1–5 are located on the ground surface $z = 0$ km. Their horizontal coordinates are (20, 20) km, (30, 20) km, (40, 20) km, (50, 20) km, and (60, 20) km, respectively

Table 1 Elastic properties of the s_1, s_2, s_3, and s_4 materials

Properties	s_1	s_2	s_3	s_4
Lamé constant λ (GPa)	18.74	36.27	50.62	81.75
shear modulus G (GPa)	15.44	37.04	46.96	65.84
density ρ (10^3 kg/m^3)	2.45	2.78	2.95	3.31
P wave velocity v_p (km/s)	4.50	6.30	7.00	8.03
S wave velocity v_s (km/s)	2.51	3.65	3.99	4.46

Validation of the computed seismic waves

At present, there are still very few quantitative studies (Yamazaki 2012; Gao et al. 2019) of the seismo-electromagnetic signals arising from the motional induction effect. Since Yamazaki (2012) did not compute the time-domain full waveforms and Gao et al. (2019) only provided 2-D solutions, our work is the first one capable of computing full waveform of seismo-electromagnetic solutions in 3-D multi-layered media due to the motional induction. Therefore, we cannot find another method to compare both seismic waves and EM signals for this exact case. However, there are many existing methods, such as finite-difference method, that can compute seismic waves for the case concerned. The curvilinear grid finite-difference method (CGFDM) has been verified to be accurate for the modeling of seismic wave propagation in solid media (Zhang and Chen 2006; Zhang et al. 2012; Sun et al. 2016, 2018). Therefore, we compare our

numerical results with those obtained from the CGFDM by considering only seismic waves.

A four-layer model (as illustrated in Fig. 1) is adopted. The four layers, from top to the bottom, consist of s_1, s_2, s_3, and s_4 materials, respectively. Their elastic properties are listed in Table 1. A double couple point source is located at (0, 0, 10) km. The spectrum of the source moment tensor $\mathbf{M}(\omega)$ can be expressed as

$$\mathbf{M}(\omega) = \begin{bmatrix} M_{xx} & M_{xy} & M_{xz} \\ M_{xy} & M_{yy} & M_{yz} \\ M_{xz} & M_{yz} & M_{zz} \end{bmatrix} \cdot s(\omega), \tag{9}$$

where M_{xx}, M_{xy}, M_{xz}, M_{yy}, M_{yz}, and M_{zz}, are the moment tensor components and $s(\omega)$ is the source time function. The adopted source is assumed to represent a fault whose strike, dip, and rake angles are 30°, 72°, and 65°, respectively. The seismic moment is set to be 5.56×10^{17} N¨m, which corresponds to a $M5.8$ earthquake. Therefore, the moment tensor components are given by: $M_{xx} = -2.67 \times 10^{17}$ N·m, $M_{xy} = 2.40 \times 10^{17}$ N·m, $M_{xz} = 1.41 \times 10^{17}$ N·m, $M_{yy} = -0.29 \times 10^{17}$ N·m, $M_{yz} = -3.89 \times 10^{17}$ N·m, and $M_{zz} = 2.96 \times 10^{17}$ N·m. In this study, the adopted source time function $s(\omega)$ is a Ricker wavelet which can be written as

$$s(\omega) = 4\sqrt{\pi}\frac{\omega^2}{(2\pi f_p)^3} e^{i\omega t_0 - \omega^2/(2\pi f_p)^2}, \tag{10}$$

where ω is the circular frequency; f_p and t_0 are the peak frequency and the time delay, respectively. For this four-layer model, we set $f_p = 1$ Hz and $t_0 = 2$ s.

Five receivers marked as triangles with specific numbers 1–5 (see Fig. 1) are considered. They are located on the ground surface $z = 0$ km and have the same y-coordinate $y = 20$ km. Their x-coordinates are $x = 20$, 30, 40, 50, 60 km. In Fig. 2, the seismic waves computed by our method (red lines) are compared with the CGFDM solutions (blue lines) for the five receivers with numbers 1–5. The three rows show the three components of seismic vibration velocity v_x, v_y, and v_z. One can find a perfect agreement between the two sets of numerical results, which, to a certain extent, verify the correctness of the semi-analytical solutions derived by Sun et al. (2021) and the validity of the numerical computation approach proposed by us.

For current problem, both the seismic and EM solutions can be regarded as summation of several inverse Hankel transforms (see Appendix A). Due to this similarity of mathematical expressions, there is a high possibility that the discrete wavenumber method and peak-trough averaging method, which have been developed for calculating seismic waves, can also be applied to compute EM fields. A more complete and convincing validation that also takes into account the computed EM signals may be carried out in the future when another method capable of computing seismo-electromagnetic solutions for 3-D multi-layered media is available.

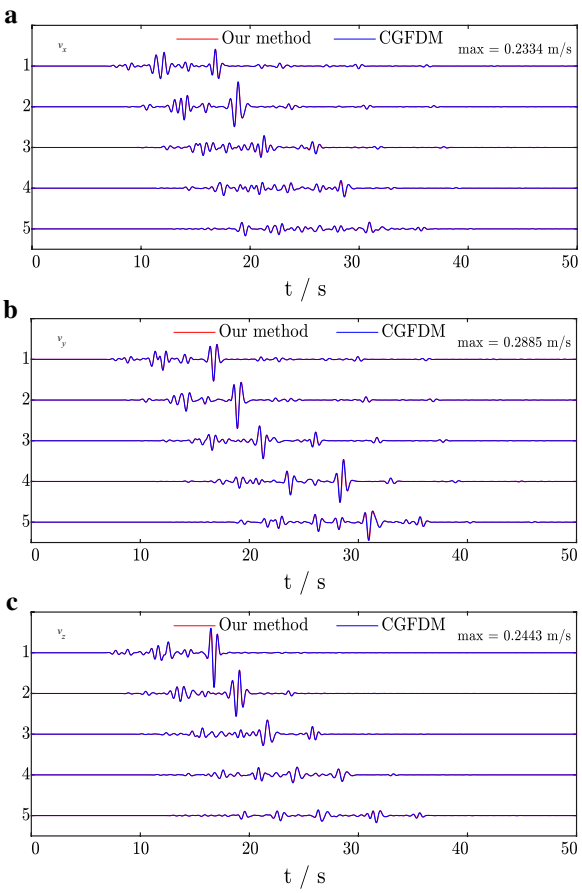

Fig. 2 Comparison of the synthetic v_x, v_y, and v_z components for the five receivers marked as triangles with specific numbers 1–5 (see Fig. 1). The read lines indicate the results computed by our method, while the blue lines indicate the numerical solutions obtained by the CGFDM

Numerical investigations

In the following section, we carry out numerical computations to investigate the characteristics of seismo-electromagnetic signals arising from motional induction. The air medium above the ground surface is assumed to be insulated and its magnetic permeability and electrical permittivity are set to be those values of the vacuum. Attenuations which are often represented by quality factors exhibit for both P and S waves in the real Earth (Press 1964). Therefore, quality factors of P and S waves (i.e., Q_p and Q_s) are considered in the following numerical

computation. Correspondingly, the slownesses of P and S waves (s_p and s_s) are calculated by following formulas:

$$s_p = \sqrt{\rho/(\lambda + 2G)}\left[1 + i/(2Q_p)\right] \tag{11}$$

$$s_s = \sqrt{\rho/G}\left[1 + i/(2Q_s)\right], \tag{12}$$

where ρ, λ and G represent density, Lamé constant and shear modulus, respectively.

Synthetic recordings of an air–solid two-layer model

To facilitate analysis, we first consider a simple model, an air–solid two-layer model, which consists of an air upper half-space and a solid lower half-space. The solid lower half-space is made up of s_5 material, whose properties are listed in Table 2. The ground surface is chosen to be the plane $z=0$ km. The source is a double couple point source located at (0, 0, 40) km. It is assumed to represent a fault with strike, dip, and rake angles of 0°, 72°, and 65°. Its seismic moment is 2.76×10^{17} N·m, which corresponds to a *M*5.6 earthquake. The ambient geomagnetic field has an intensity of 5×10^{-5} T. Its inclination and declination angles are 45° and 10°, respectively. The source time function is a Ricker wavelet with a peak frequency of 0.8 Hz and a time delay of 2.5 s. Seismo-electromagnetic signals are checked for two receivers nearby the ground surface. One is buried 0.1 m underground, while the other one is 2 m above the ground surface. Both of the two receivers have the same horizontal coordinates of $x=95.76$ km and $y=80.35$ km.

Figure 3 shows the seismic vibration velocity (v_x, v_y and v_z), electric field (E_x, E_y and E_z), and magnetic induction intensity (B_x, B_y and B_z) computed for the underground receiver (yellow lines), as well as EM signals (E_x, E_y, E_z, B_x, B_y, and B_z) calculated for the other receiver in the air (thin blue lines). In exception to the E_z components, the other five EM components (E_x, E_y, B_x, B_y, and B_z) are continuous across an interface. Besides, the two receivers are close enough, since their distance is negligible compared with the seismic wavelength. As a result, an overlap of the yellow and blue lines occurs for those five EM components (E_x, E_y, B_x, B_y, and B_z). Seismic arrivals of P and S waves, which start to show up at ~ 24.5 s and ~ 42 s, respectively, are obvious in both seismic and EM signals. Therefore, the EM signals displayed in Fig. 3 show up simultaneously with seismic arrivals. They are the so-called coseismic EM signals. This numerical result confirms that the motional induction effect is one of the possible generation mechanisms of coseismic EM signals associated with natural earthquakes (Iyemori et al. 1996; Honkura et al. 2000, 2004; Matsushima et al. 2002; Ujihara et al. 2004; Tang et al. 2010). Since the blue lines (in Fig. 3) correspond to the receiver above the ground surface, our numerical results suggest that coseismic EM signals can be recorded by receivers in the air. Actually, such a phenomenon was already reported in field observation by Ujihara et al. (2004). They set up induction coils hung in the air between trees to record magnetic signals. The observed magnetic field after band-pass filtering operation also exhibited the coseismic characteristic. Therefore, our computational result indicates that motional induction effect could be one of the possible generation mechanisms for the coseismic magnetic signals recorded in the Earth's near-surface air (Ujihara et al. 2004). Other possible generation mechanisms include the electrokinetic effect, the piezomagnetic effect and so on. Further efforts to validate this idea could be made in the future.

Table 2 Properties of the s_5, s_6, s_7, s_8, s_9, s_{10}, and s_{11} materials

Properties	s_5	s_6	s_7	s_8	s_9	s_{10}	s_{11}
Lamé constant λ (GPa)	26.38	6.92	27.67	27.67	36.94	48.36	71.27
Shear modulus G (GPa)	27.65	0.88	30.4	30.4	35.91	45.33	58.34
Density ρ (10^3 kg/m^3)	2.7	1.97	2.63	2.63	2.74	2.92	3.17
P wave velocity v_p (km/s)	5.5	2.1	5.8	5.8	6.3	6.9	7.7
S wave velocity v_s (km/s)	3.2	0.67	3.4	3.4	3.62	3.94	4.29
P wave quality factor Q_p	500	200	320	320	400	450	500
S wave quality factor Q_s	200	80	130	130	160	180	200
Conductivity σ (S/m)	0.001	0.01	1	0.001	0.001	0.001	0.001
Relative electrical permittivity ε_r	10	6	15	4	4	4	4
Relative magnetic permeability μ_r	1	1	1	1	1	1	1

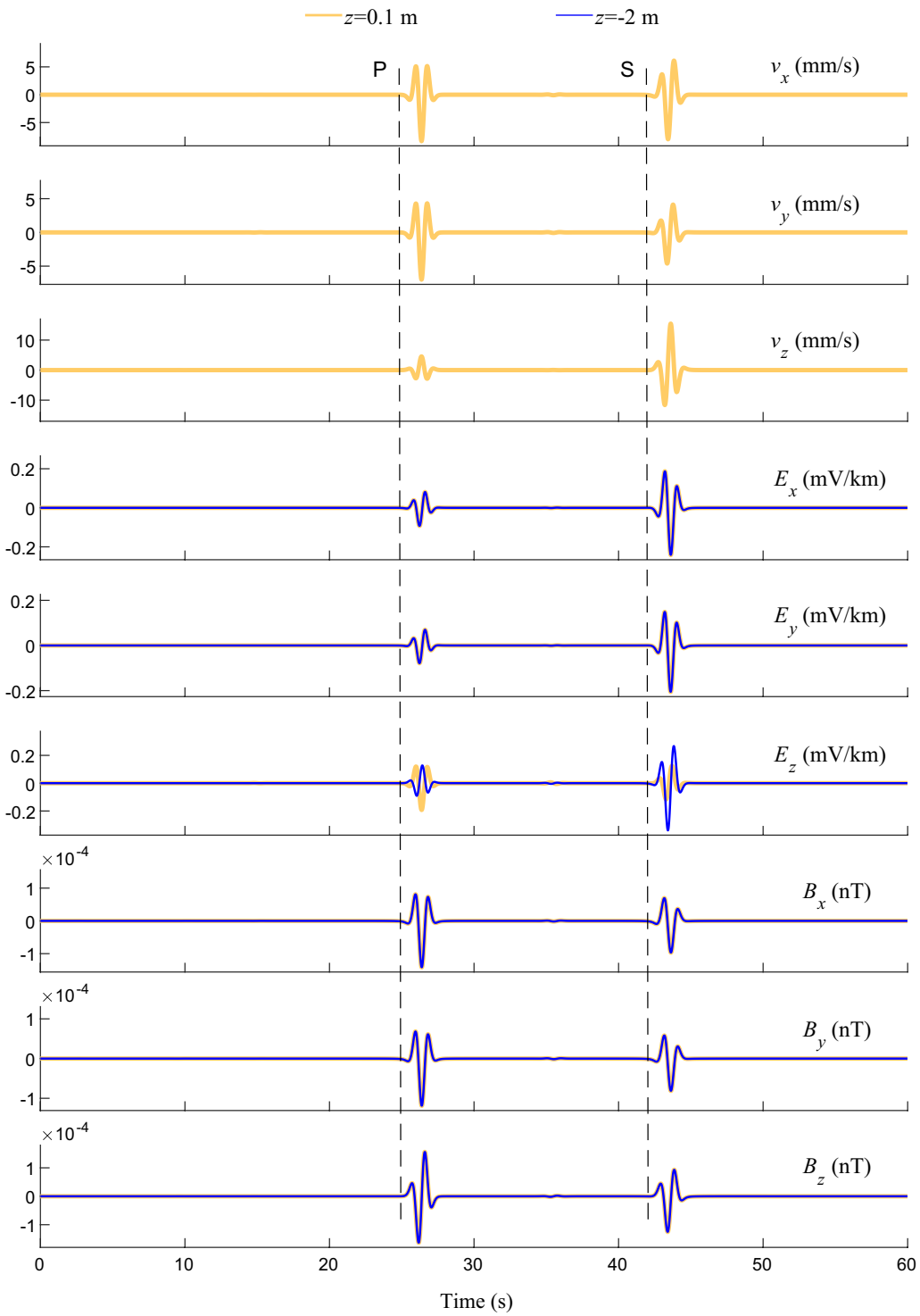

Fig. 3 Seismo-electromagnetic signals computed for two receivers nearby the ground surface of an air–solid two-layer model. Seismic vibration velocity (v_x, v_y and v_z), electric field (E_x, E_y and E_z), and magnetic induction intensity (B_x, B_y and B_z) computed for the underground receiver at (95.76, 80.35, 0.0001) km are indicated by the yellow lines, whereas the blue lines display the EM signals (E_x, E_y, E_z, B_x, B_y, and B_z) computed for the other receiver at (95.76, 80.35, − 0.002) km, that is, 2 m above the ground surface

Wave-field snapshots

Still using the air–solid two-layer model, we investigate the propagation of the seismic and EM wavefields by computing snapshots at different times for a rectangular area that has an epicentral (radial) distance range from 0 to 100 km, an azimuthal angle of 40°, and a depth range from − 5 to 15 km. The wave-field snapshots are determined at 401×81 receiver positions. The receiver spacing is 0.25 km in either epicentral (radial) direction or vertical direction.

Figure 4 displays the snapshots of seismic vibration velocity v_x component at times of 10.23, 14.23, 18.23,

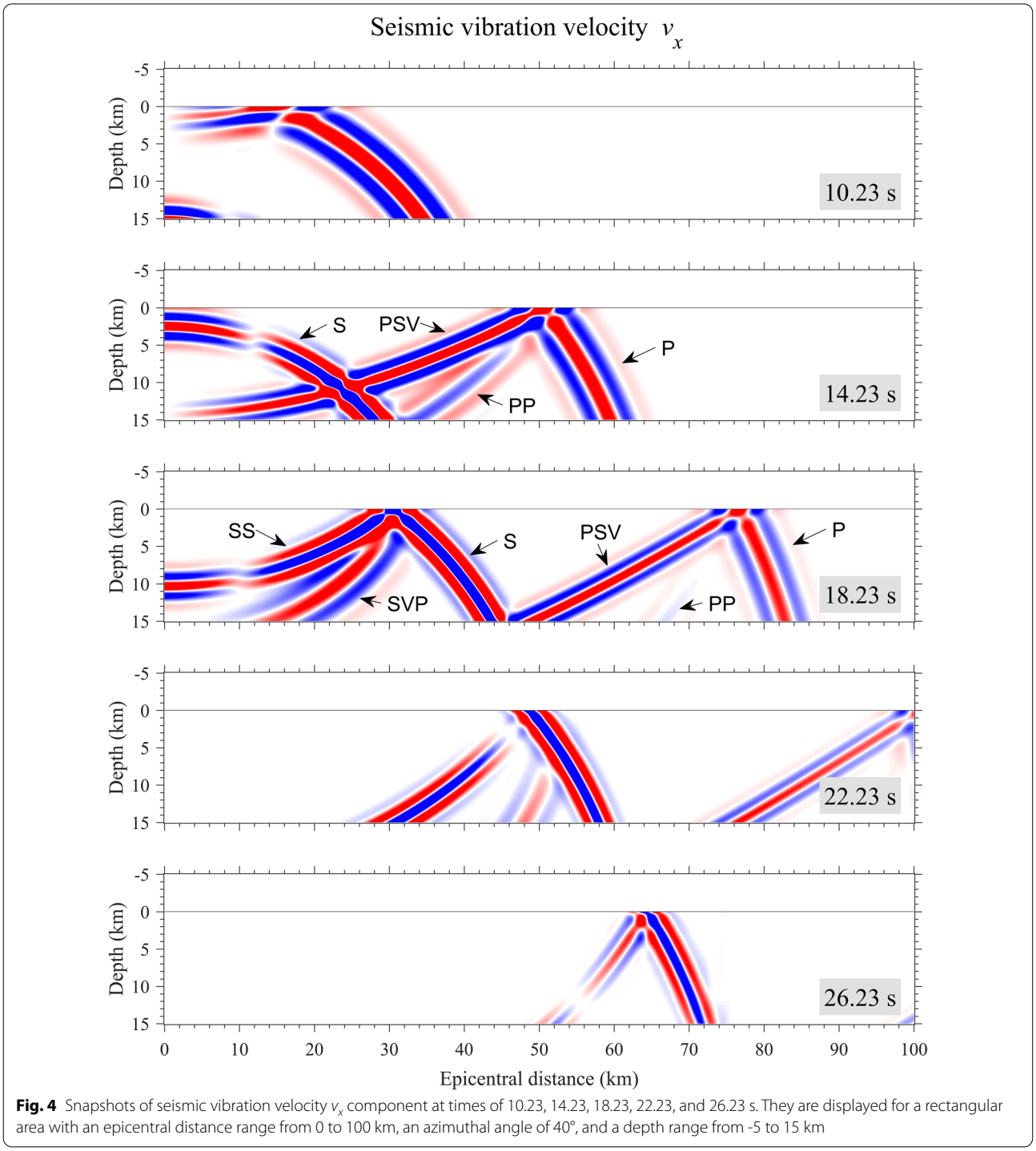

Fig. 4 Snapshots of seismic vibration velocity v_x component at times of 10.23, 14.23, 18.23, 22.23, and 26.23 s. They are displayed for a rectangular area with an epicentral distance range from 0 to 100 km, an azimuthal angle of 40°, and a depth range from -5 to 15 km

22.23, and 26.23 s. In the top snapshot (i.e., at the time of $t=10.23$ s), the direct S wave is still propagating upward, whereas the direct P wave has arrived at the ground surface ($z=0$ km) giving birth to the reflected PP and PSV waves that start to propagate downward. At the time of $t=14.23$ s (the second snapshot), the direct S wave just reaches the ground surface and the reflected PP and PSV waves are separated from each other, since they have propagated downward for a while. The third snapshot ($t=18.23$ s) exhibits the SS and SVP waves reflected downward off the ground surface in addition to the direct P and S waves and reflected PP and PSV waves. The signal strength of the reflected PP wave becomes much weaker in comparison with other waves. In the bottom two snapshots computed at times of $t=22.23$ s and $t=26.23$ s, all the waves further propagate outward as time elapses.

Under the ambient geomagnetic field $\mathbf{B^a}$, seismic vibration in a conductive medium gives birth to the induction electric current $\sigma\mathbf{v}\times\mathbf{B^a}$, where σ and $\mathbf{v}$ are the material conductivity and the seismic vibration velocity, respectively. This induction electric current causes accumulation and depletion of electric charges that naturally result in an electric field. Under this electric field, electric charges has to move forming the conductive current $\sigma\mathbf{E}$. In a homogeneous medium, the induction electric current and the conductive current will be counterbalanced by each other and an equilibrium will be reached eventually. The curl electric field will further generate magnetic field. Therefore, EM fields accompanying seismic waves will be induced in a conductive medium. They are local responses to the seismic waves passing by and hence can be called localized EM fields.

Figures 5 and 6 show the snapshots of electric field E_x component and magnetic field B_x component, respectively, for the same times and the same area as Fiugre 4. For the area below the ground surface, one can easily identified part of the localized electric field, which accompanies the S waves (including the direct S wave, the reflected PSV wave and the reflected SS wave), as well as the localized magnetic field, which accompanies all seismic waves. The localized electric field accompanying the P waves (including the direct P wave, the reflected PP wave and the reflected SVP wave) actually also exists but its signal strength is much weaker than those associated with the S waves. The cause of this result is that of the solid half-space (s_5 material) has a conductivity of 0.001 S/m. For such a conductivity value, Gao et al. (2014) showed that the localized electric field of P waves could be more than two orders of magnitude weaker than that of S waves at the frequency of 1 Hz. Hence, the signal strength characteristic of the localized electric field in Fig. 5 is consistent with the analysis of Gao et al. (2014). Besides, Gao et al. (2014) also showed that the P and S waves' capacity of inducing localized electric field generally become closer when the conductivity increases from 0.0001 to 1 S/m for a frequency of 0.1, 1, 10, or 100 Hz. We also computed the snapshots by changing the conductivity of the solid half-space to 0.1 S/m. For that case, the localized electric field associated with both P and S waves can be clearly identified. The snapshots of that case are not displayed here to save space.

The localized EM fields exist in the solid but is absent in the air. Thus, they cannot be continuous across the ground surface. To satisfy the EM boundary condition, i.e., the continuity requirement of the total EM tangential components at an interface, corresponding non-localized EM fields are then generated. As a result, EM fields can also be observed in the air. Those in-air EM fields decay rapidly when moving away from the ground surface (see Figs. 5 and 6).

If we use k to indicate the horizontal wavenumber of seismic waves arriving at the ground surface, the localized EM fields will have the same horizontal wavenumber, which is given by $k=\sin\theta(\omega/V_{\mathrm{sei}})$, where V_{sei} is the seismic wave velocity, and θ is the incident angle of the seismic waves arriving at the ground surface. Thereafter, as a result of the continuity boundary condition of EM fields at the ground surface, the horizontal wavenumber of non-localized EM fields in the air should also be equal to k. This means the horizontal wavenumber also satisfies the equation $k^2-(\gamma_{\mathrm{em}})^2=(\omega/V_{\mathrm{em}})^2$, where V_{em} is the speed of light when we consider the EM fields in the air and $\gamma_{\mathrm{em}}=\sqrt{k^2-(\omega/V_{\mathrm{em}})^2}$ is i times the vertical wavenumber of the non-localized EM fields. There is no down-going EM fields in the top layer (i.e., in the air); thus, a depth-dependent factor $\exp(\gamma_{\mathrm{em}}z_{\mathrm{rcv}})$ (where z_{rcv} indicates the depth of an in-air receiver, i.e., $-z_{\mathrm{rcv}}$ represents the distance from an in-air receiver to the ground surface $z=0$ m) exists for the non-localized EM fields (Sun et al. 2021). Since seismic wave velocity is much lower than the speed of light, there is a high possibility that the value of k exceeds the value of ω/V_{em}. Thus, there is a critical incident angle θ_c satisfying

$$\theta_c=\arcsin(V_{\mathrm{sei}}/V_{\mathrm{em}}). \tag{13}$$

If $\theta\le\theta_c$, γ_{em} will be an imaginary number and the corresponding non-localized EM fields will be radiation EM waves. If $\theta>\theta_c$, then we obtain $k>\omega/V_{\mathrm{em}}$ and γ_{em} is a positive real number. Thus, the depth-dependent factor $\exp(\gamma_{\mathrm{em}}z_{\mathrm{rcv}})$ represents an exponential decay suggesting the corresponding non-localized EM fields will be evanescent waves whose amplitudes decay rapidly along the normal direction of the interface.

The speed of light usually could be 5 orders of magnitude greater than the seismic velocity V_{sei}. Consequently, the critical incident angle θ_c is a very small

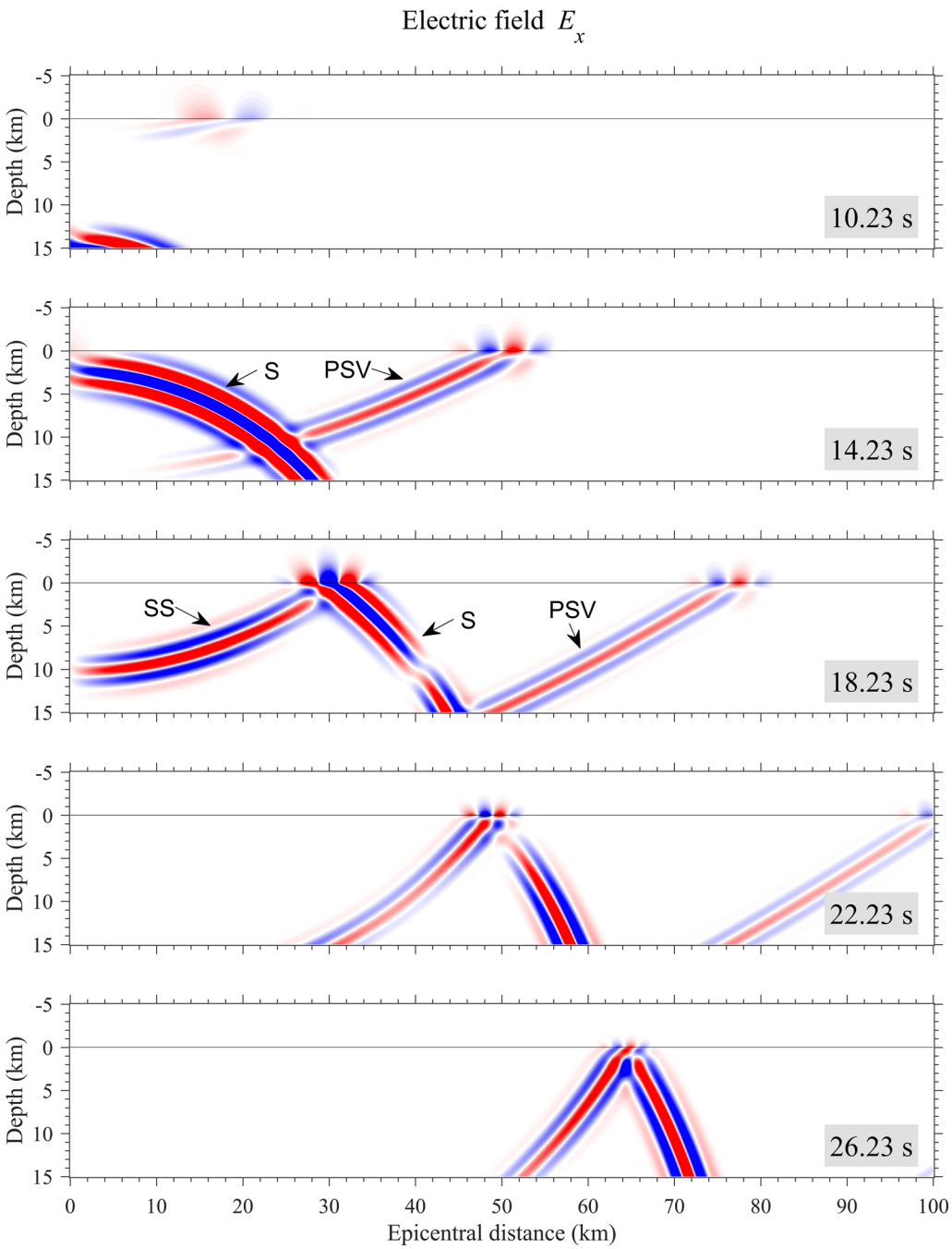

Fig. 5 Snapshots of electric field E_x component computed for the same times and the same area as Fig. 4

value suggesting only the seismic waves with a nearly normal incident angle can generate radiation EM waves. We call them interfacial radiation EM waves, because they result from the seismic-to-EM conversion at an interface. Another kind of direct radiation EM waves can be directly converted from the earthquake source (Gao et al. 2014). For a receiver in non-epicentral area, both the direct and the interfacial radiation EM waves can arrive earlier than seismic P wave by several seconds or more, because they propagate with EM wave velocity. However, these radiation EM waves are so weak that they are usually invisible in the EM signals (see Fig. 3). Some 2-D numerical investigations of

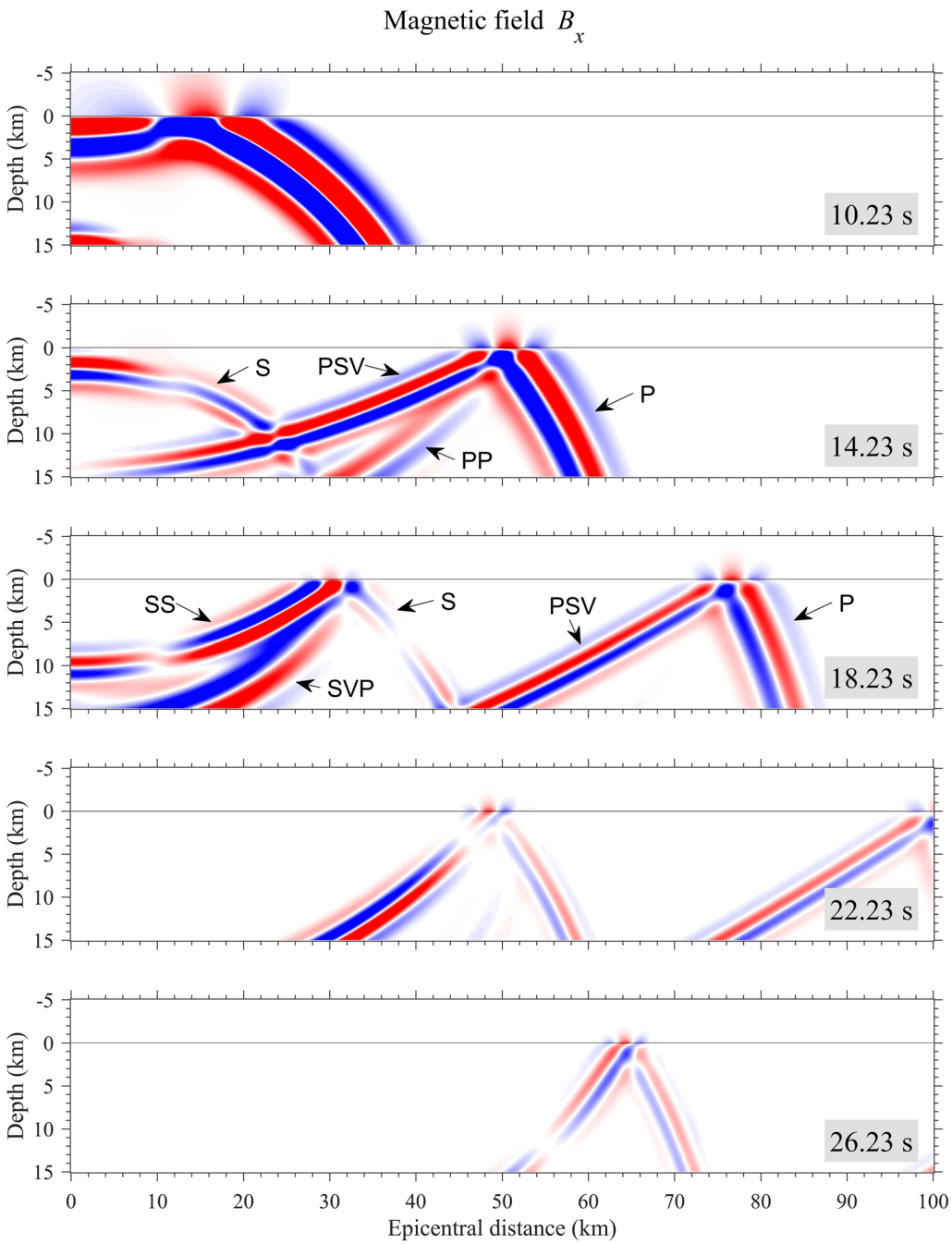

Fig. 6 Snapshots of magnetic field B_x component computed for the same times and the same area as Fig. 4

the radiation EM waves caused by motional induction effect were conducted by Gao et al. (2019).

For the non-epicentral area on the ground surface, the incident angles of seismic waves are usually large enough and evanescent EM waves are induced. Therefore, the in-air EM fields shown in Figs. 5 and 6 are mainly contributed by evanescent EM waves. It should be mentioned the evanescent EM waves are also induced at the lower side of the ground surface, but they can hardly be identified unless separated from the localized EM fields.

Considering the electrokinetic effect, seismo-electromagnetic signals caused by an earthquake source have been numerically investigated in the last two decades (e.g., Pride et al. 2004; Hu and Gao 2011; Ren et al. 2012,

2016a; Zhang et al. 2013; Huang et al. 2015; Sun et al. 2019). The evanescent EM waves arising from the electrokinetic effect was identified for the first time by Ren et al. (2016a). Based on further numerical modellings, Ren et al. (2016b) proposed the electrokinetically generated evanescent EM waves have significant contribution to the coseismic EM signals. This idea was later adopted by Dzieran et al. (2019), who used observational data of coseismic electric signals generated by natural earthquakes to analyze the frequency-domain seismoelectric spectral ratio, i.e., the ratio of observed electric field to the seismic ground acceleration. They found the seismoelectric spectral ratio showed a decreasing characteristic for increasing frequency and this characteristic cannot be reasonably explained unless the evanescent EM waves were taken into consideration. Recently, Ren et al. (2020) further proposed evanescent EM waves can also be generated by motional induction effect or other seismo-electromagnetic coupling mechanisms. Now, this viewpoint is confirmed at least for the motional induction effect, because the generation of evanescent EM waves due to the motional induction effect can be deduced from the semi-analytical solutions (Sun et al. 2021) if one notices that the EM field expansion coefficients contain factors like $\exp(\gamma_{em} z_{rcv})$ (for an in-air receiver), in which $\gamma_{em} = \sqrt{k^2 - \omega^2/V_{em}^2}$ ($\mathrm{Re}\{\gamma_{em}\} > 0$ is defined when γ_{em} has a non-zero real part). The numerical results in Figs. 5 and 6 also provide supporting evidence.

Amplitude decay characteristic

The amplitude decay characteristic of evanescent EM waves can be used to verify the validity of our computation approach. Still using the air–solid two-layer model, we compute EM fields for 16 receivers in the air, which are evenly spaced in a vertical line segment with coordinates of $x = 95.76$ km, $y = 80.35$ km and $-1.5 \le z \le 0$ km. As shown in Fig. 7, all the EM components include two groups of signals showing up around 26 s and 44 s, respectively, which are the times when P and S waves arrive at the position (95.76, 80.35, 0) km. They exhibit an amplitude decay characteristic for increasing distance from the receiver to the ground surface. These EM signals actually are the evanescent EM waves, since these receivers are obviously located in a non-epicentral area. As illustrated in Appendix B, the evanescent EM waves have an amplitude decay factor f_{decay} related to circular frequency ω, seismic incident angle θ, seismic wave velocity V_{sei}, and the depth of an in-air receiver z_{rec} as

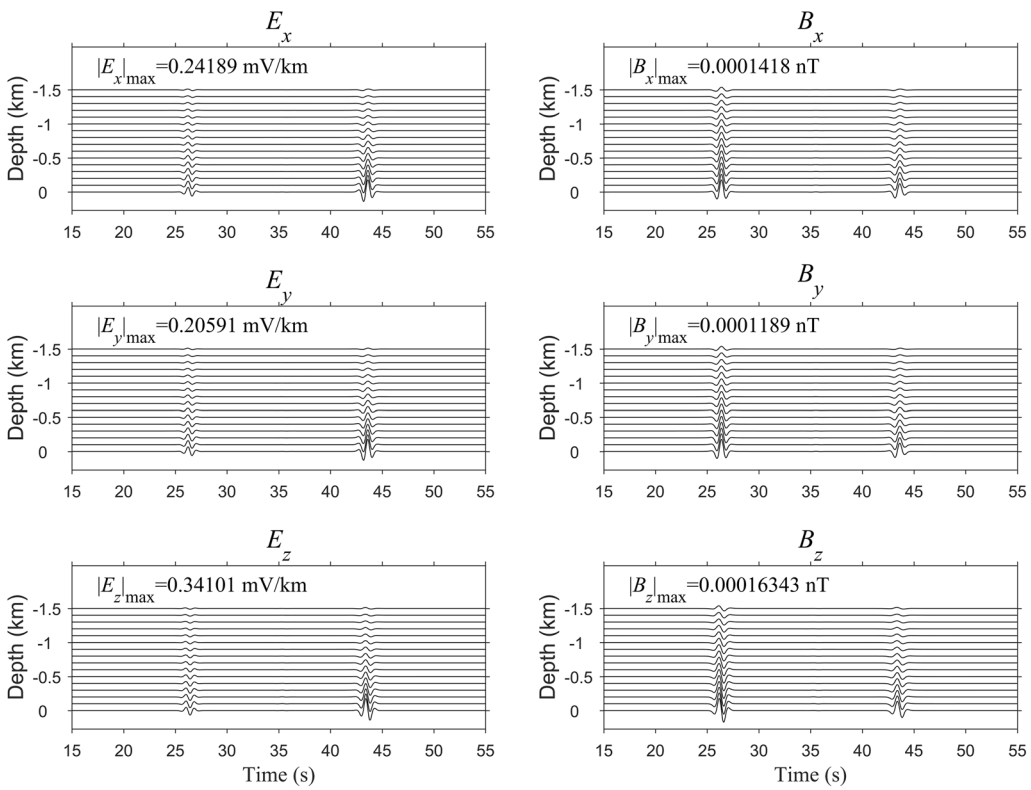

Fig. 7 EM fields in the air computed for 16 receivers evenly spaced in a vertical line segment with coordinates of $x = 95.76$ km, $y = 80.35$ km and $-1.5 \le z \le 0$ km

$$f_{\text{decay}}(\omega, z) \approx \exp\left(\omega \frac{\sin\theta}{V_{\text{sei}}} z_{\text{rcv}}\right). \tag{14}$$

Further investigations are carried out to check whether the synthetic EM signals displayed in Fig. 7 have the decay characteristic described by equation (14). These signals are filtered by a frequency-domain Hanning function that can be written as

$$R_{\text{filter}}(f) = \begin{cases} 0, & f \le f_1 \\ 0.5 - 0.5\cos[2\pi(f - f_1)/(f_2 - f_1)], & f_1 < f < f_2 \\ 0, & f \ge f_2 \end{cases}. \tag{15}$$

where f_1 and f_2 are the cutoff frequencies. After filtering, the frequency component at $f = 0.5(f_1 + f_2)$ will remain the same, while the other frequency components will be suppressed.

Figure 8 shows one group of EM signals, which are induced by direct P waves and filtered by the Hanning function at $0.72 < f < 0.88$ Hz. The signals in the left two plots are normalized by the maximum amplitude of all receivers' synthetic recordings. In Fig. 8(c), the maximum amplitude of each receiver is normalized by the corresponding maximum amplitude of the ground surface receiver, i.e., the one located at (95.76, 80.35, 0) km. The solid line with dot mark and the dashed line with square mark denote the amplitude decay speed of the simulated E_x and B_y signals, respectively. The yellow line is the theoretical decay curve determined by

$$f_{\text{decay}} = \exp(8.7044 \times 10^{-4} z_{\text{rcv}}), \tag{16}$$

where 8.7044×10^{-4} is the value determined by the peak frequency 0.8 Hz, the incident angle 0.4014π (which is determined by arctan(125/40), since the ground surface receiver has an epicentral distance of 125 km and the focal depth is 40 km), and the P wave velocity of the solid half-space. Obviously, the decay curves of E_x and B_y are overlapped with the theoretical decay curve. A similar situation is shown by Fig. 9 for another group of EM signals, which are induced by direct S waves and whose theoretical decay curve is given by

$$f_{\text{decay}} = \exp(14.9606 \times 10^{-4} z_{\text{rcv}}). \tag{17}$$

Therefore, the computed EM signals in air show an excellent agreement with the theoretically predicted amplitude decay characteristic for a single frequency and single wavenumber. This fact might be regarded as a special validation of the EM fields computed by the proposed numerical approach.

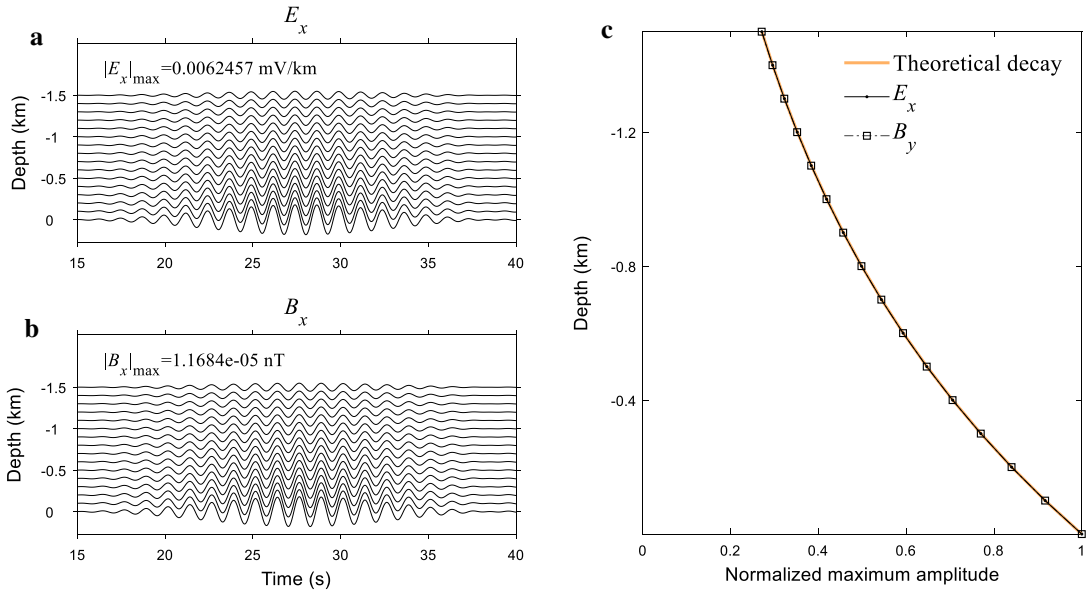

Fig. 8 Synthetic recordings of **a** electric field component E_x and **b** magnetic field component B_x, which are induced by the direct P waves and filtered by a Hanning function at $0.72 < f < 0.88$ Hz. **c** The amplitude decay curves of the simulated EM signals (E_x and B_x) in comparison with the theoretical decay curve determined by $f_{\text{decay}} = \exp(8.7044 \times 10^{-4} z_{\text{rcv}})$, where z_{rec} represents the depth of an in-air receiver

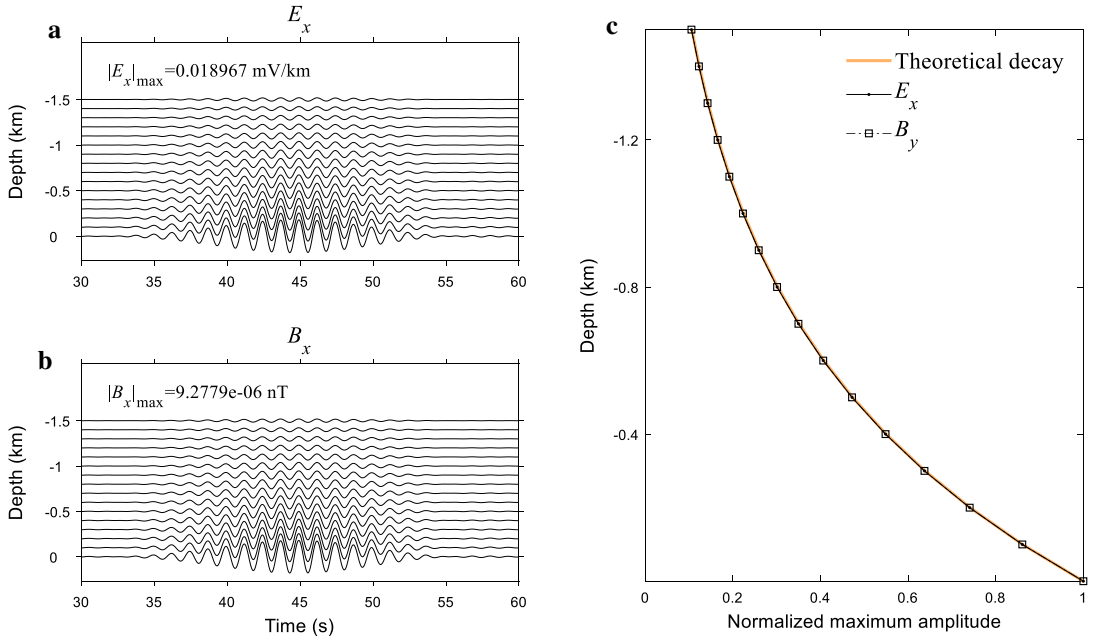

Fig. 9 Synthetic recordings of **a** electric field component E_x and **b** magnetic field component B_x, which are induced by the direct S waves and filtered by a Hanning function at $0.72 < f < 0.88$ Hz. **c** The amplitude decay curves of the simulated EM signals (E_x and B_x) in comparison with the theoretical decay curve determined by $f_{decay} = \exp(14.9606 \times 10^{-4} z_{rcv})$, where z_{rec} represents the depth of an in-air receiver

Influence of conductivity at depth

For receivers located in the shallow subsurface (e.g., at a depth of 0.1 m), which could be a common situation in field survey, the amplitude of the recorded EM fields will be affected by the conductivity of the medium in which the receivers are located, because the induction electric current $\sigma \mathbf{v} \times \mathbf{B^a}$, which acts as the source in the Maxwell's equations to generate EM fields, is evidently influenced by the conductivity σ. The amplitudes of the EM fields generally increase for a higher conductivity of the shallow subsurface. This point was already verified by Yamazaki (2012) and Gao et al. (2019). In this section, we investigate another interesting but unexamined question: how the conductivity at depth affects the waveforms of the EM fields recorded by receivers in the shallow subsurface?

The adopted model is modified from the air–solid two-layer model used in the above by enhancing the conductivity of the solid medium in the depth range of $200 \le z \le 600$ m. This makes it a high conductive layer, which often exists in the Earth's crust. We use σ_2 to indicate the enhanced conductivity. Figure 10 shows the EM fields computed for a receiver located at (95.76, 80.35, 0.0001) km, i.e., in the shallow subsurface, when σ_2 is set to be 0.1, 0.3, and 0.9 s/m, respectively. The computed seismic signals are the same as those shown as yellow lines in the top three rows of Fig. 2, because the elastic properties are unchanged. The EM signals showing up around 26 and 44 s in Fig. 10 are the coseismic signals associated with direct P and S waves, respectively. All the three magnetic components (B_x, B_y, and B_z) show an obvious and uniform variation trend, that is, enhanced amplitude for higher σ_2. However, the behavior of the electric field is kind of disordered. The coseismic E_x signals around 26 s exhibit first a slight amplitude decrease for σ_2 changed from 0.1 S/m to 0.3 S/m and then an amplitude increase for σ_2 further changed to 0.9 S/m. For these signals, a waveform variation along with the change of σ_2 takes place and a phase reversal can be observed between the result of $\sigma_2 = 0.1$ S/m and $\sigma_2 = 0.9$ S/m. The coseismic E_x signals around 44 s seemingly display a variation trend of decreasing amplitude for higher σ_2. The signal strength of the coseismic E_y component is generally enhanced for higher σ_2, but its amplitude variation is less dramatic than those of the three magnetic components. For the coseismic E_z component, neither the amplitude nor the waveform shows evident variation.

Summing up the above, in exception to the E_z component, the EM fields are obviously influenced by the conductivity at depth. Such kind of influence actually results from the evanescent EM waves. For a subsurface interface of conductivity contrast, the localized EM fields are discontinuous, and thus interfacial radiation EM waves and evanescent EM waves are induced to satisfy EM

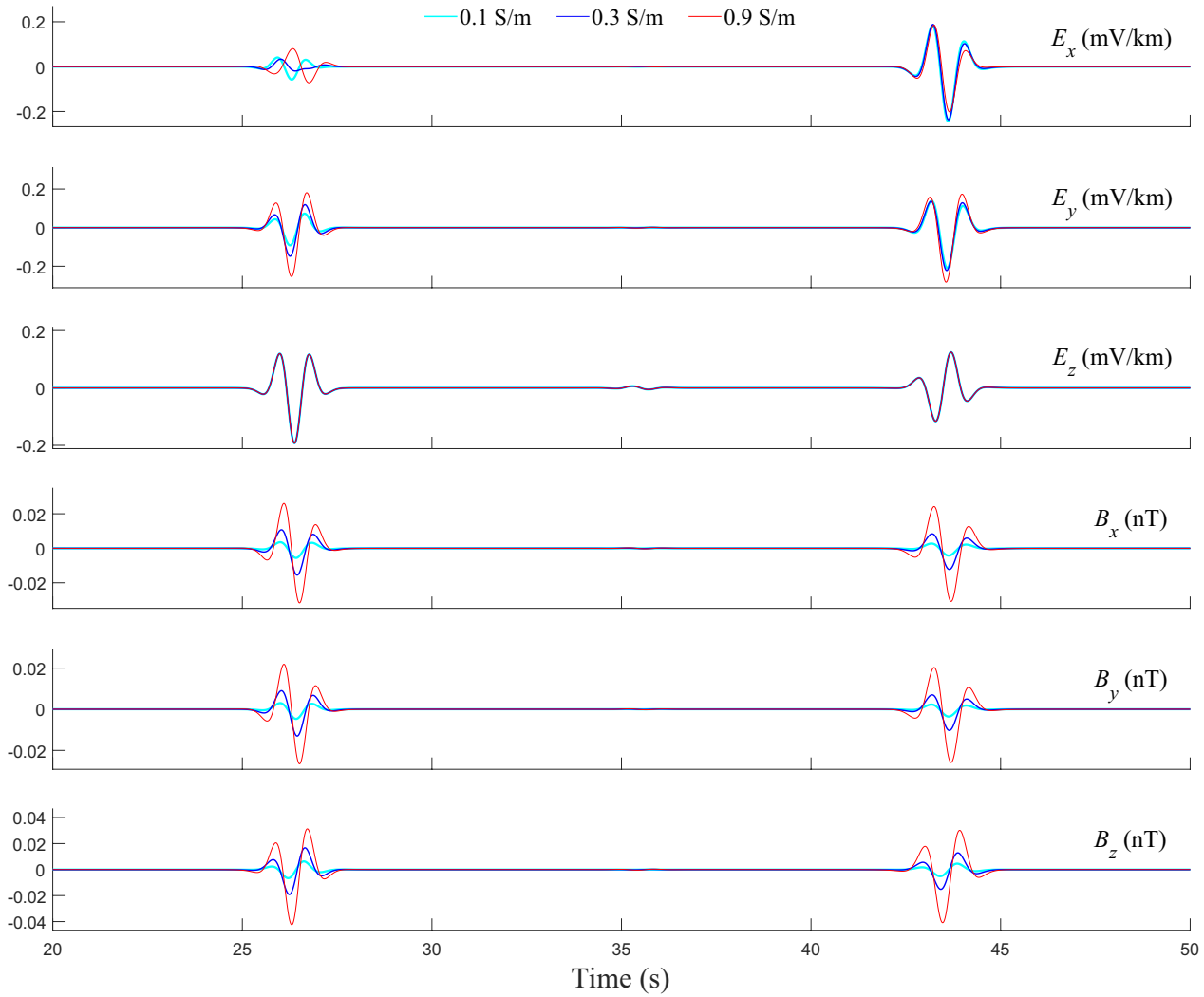

Fig. 10 EM fields computed for a receiver located in the shallow subsurface when σ_2, the conductivity of the solid medium in the depth range of $200 \leq z \leq 600$ m, is set to be 0.1, 0.3, and 0.9 s/m, respectively

fields' continuity boundary condition. The evanescent EM waves will go through amplitude decay along the normal direction of the interface and be recorded by the receiver nearby the ground surface. When the subsurface interface is close to the ground surface, i.e., the distance between them is relatively small in comparison with seismic wavelength, the evanescent EM waves will seemingly accompany seismic waves and contribute to the coseismic EM fields. Therefore, the conductivity at depth affects the coseismic EM fields through the evanescent EM waves generated at subsurface interfaces. Yamazaki (2012) considered only Rayleigh waves and also showed that the conductivity at depth can influence the magnetic field. That result can also be explained by the evanescent EM waves.

Dealing with fault rupture spreading to the ground surface

For a shallow-focus big earthquake, fault rupture spreading to the ground surface often happens and causes devastating destructions. Such case has not been considered in previous numerical investigations of seismo-electromagnetic signals (e.g., Hu and Gao 2011; Ren et al. 2012). We now adopt a model of such case and use our numerical computation approach, which combines discrete wavenumber method, peak-trough averaging method, and point source stacking method, to compute the seismo-electromagnetic signals.

The adopted model (see Fig. 11) is made up of an air layer and six solid layers consisting of s_6, s_7, s_8, s_9, s_{10}, and s_{11} materials, whose properties are listed in Table 2. This

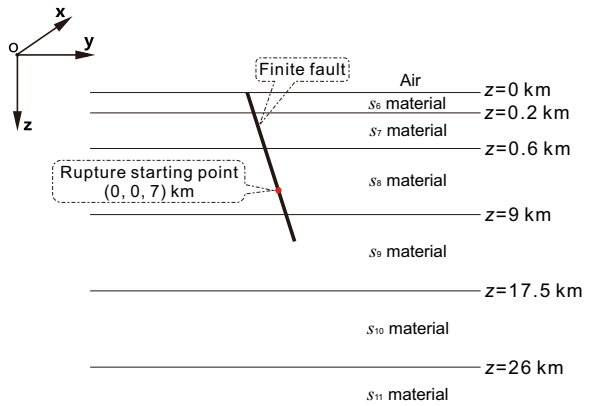

Fig. 11 Side view along *x*-direction of a seven-layer model. It consists of an air layer and six solid layers. A finite fault penetrates the top four solid layers and touches the ground surface

seven-layer model is designed by referring to CRUST 1.0 for the velocity structure at the location of (32.5°N, 130.5°E). The second and third solid layers (made up of s_7 and s_8 materials) have the same elastic properties but different electric properties. The earthquake source is a rectangular finite fault of 20×12.6175 km^2 penetrating the top four solid layers. Its strike, dip, and rake angles are 0°, 72°, and 65°, respectively. Distribution of the maximum slip displacement on the fault plane is displayed in Fig. 12. The fault rupture starts from the position of (0, 0, 7) km, propagates in the fault plane with a constant speed 2.7 km/s, and spreads to the ground surface. Its seismic moment is 4.65×10^{18} N¨m, which corresponds to a M6.4 earthquake. Once again, the source time function is set to be a Ricker wavelet with a peak frequency of 0.8 Hz and a time delay of 2.5 s. Referring to the data of IGRF13 (Alken et al. 2021) for the geomagnetic field at (32.5°N, 130.5°E), we set an ambient geomagnetic field with an intensity of 4.74786×10^{-5} T, an inclination angle of 47.15°, and a declination angle of − 7.3°. The receiver is located at (76.60, 64.28, 0.0001) km.

Adopting the point source stacking method, we discretize the finite fault into 100×60 cells. The seismic and EM signals generated by each cell are computed by jointly using the discrete wavenumber method and peak-trough averaging method. The finally obtained seismic and EM wavefields are displayed in Fig. 13. Compared with the computational result of the air–solid two-layer model (Fig. 3), the waveforms of both seismic and EM signals become more complicated, which is surely reasonable because of the multiple reflections occurring on the interfaces. The computational time of this model is about

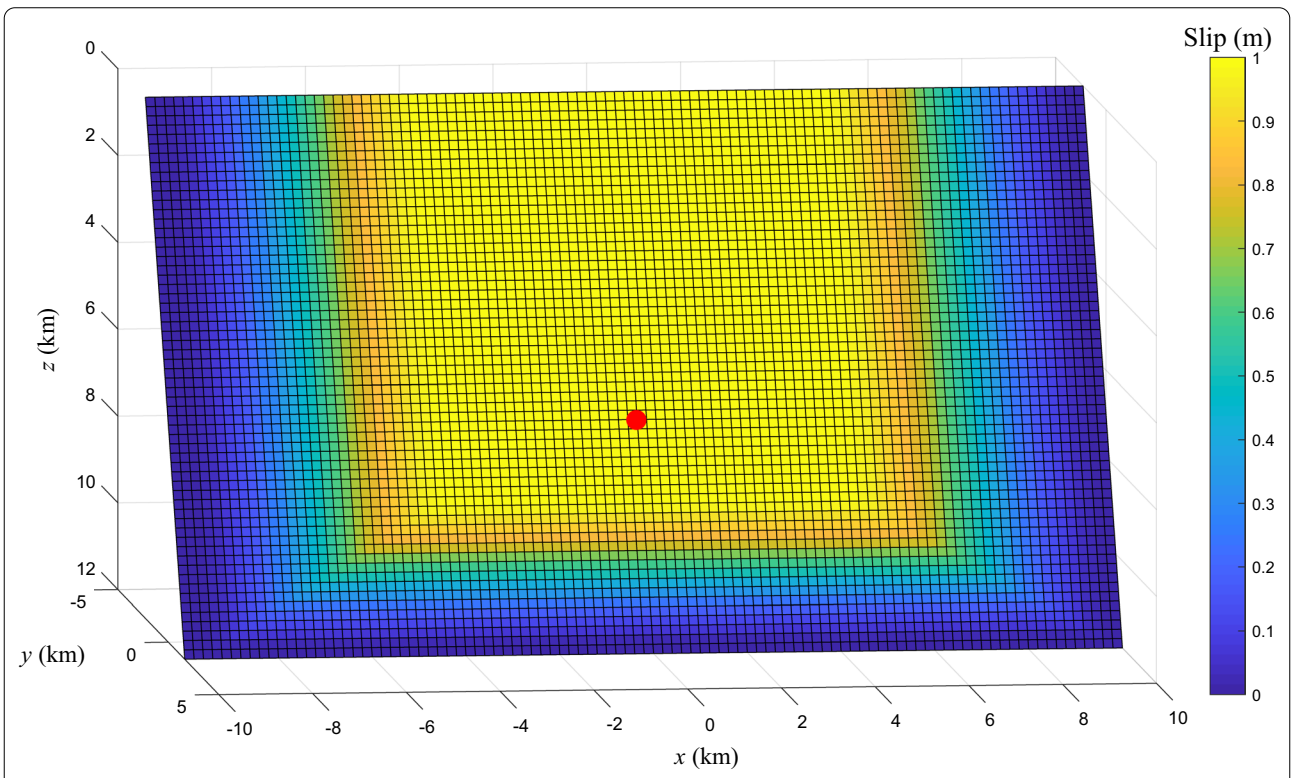

Fig. 12 Distribution of the maximum slip displacement on the fault plane. The red point indicates the rupture starting point which is located at (0, 0, 7) km

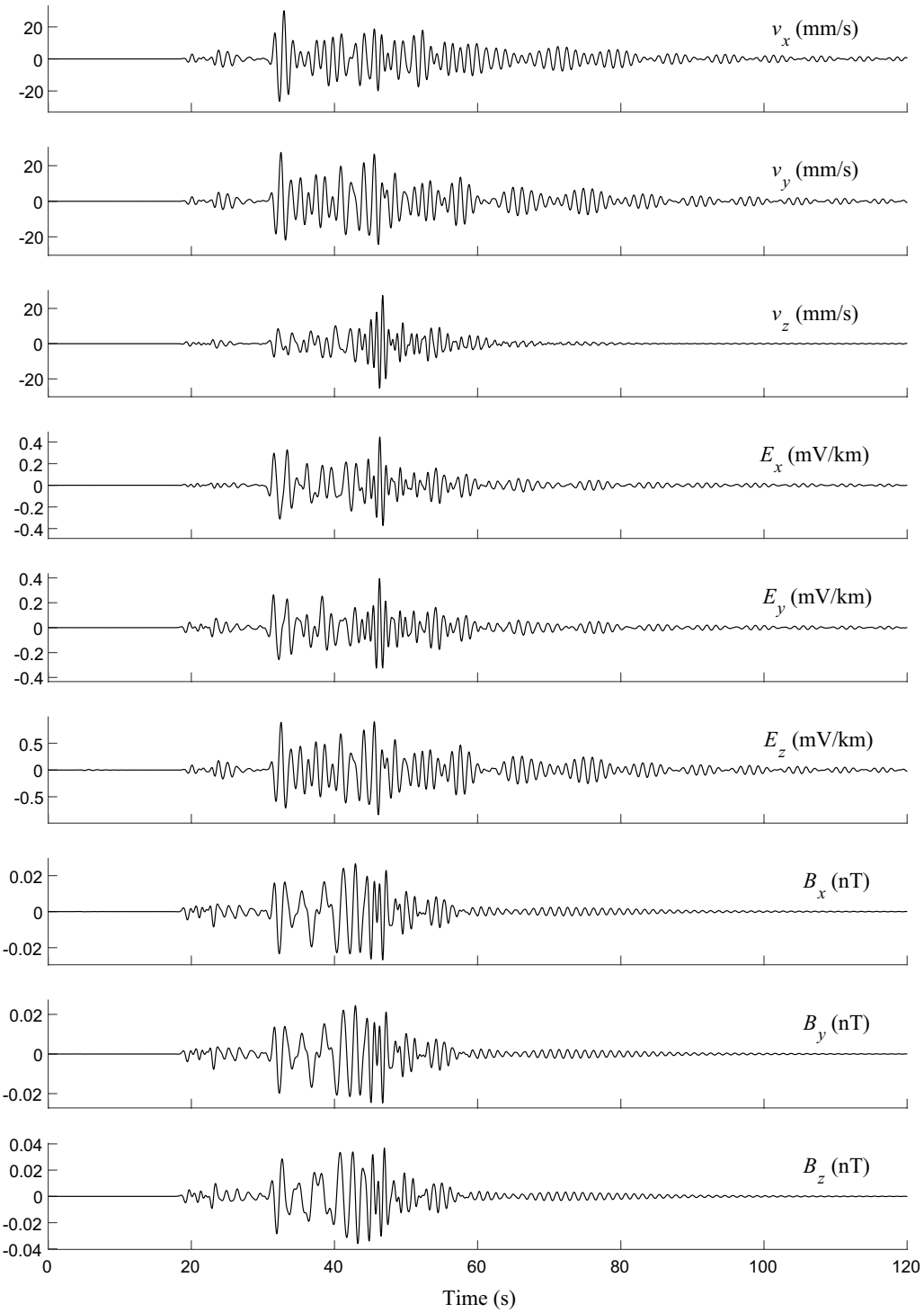

Fig. 13 Seismic vibration velocity (v_x, v_y and v_z), electric field (E_x, E_y and E_z), and magnetic induction intensity (B_x, B_y and B_z) computed for a receiver located at (76.60, 64.28, 0.0001) km in the seven-layer model

7.4 h when a 72-worker parallel computation is implemented on Matlab platform. Generally speaking, the EM fields in Fig. 13 still exhibit the coseismic characteristic, which once again demonstrates the motional induction effect is likely to contribute to the coseismic EM signals recorded during natural earthquakes (Iyemori et al. 1996;

Honkura et al. 2000, 2004; Matsushima et al. 2002; Ujihara et al. 2004; Tang et al. 2010).

Conclusions

In this study, a numerical computation approach is introduced on basis of the semi-analytical solutions of Sun et al. (2021) to calculate seismo-electromagnetic signals arising from the motional induction effect due to a double couple point source or a finite fault embedded in a 3-D multi-layered media. The accuracy and reliability of the proposed method is partially verified by the comparison with CGFDM for the seismic waves propagating in a multi-layered media. The existence of the evanescent EM waves resulting from the motional induction effect is identified and the influence of the conductivity at depth to the coseismic EM signals is demonstrated. Our numerical results support the viewpoint that motional induction effect is a possible explanation of the coseismic EM phenomena observed during earthquakes (Iyemori et al. 1996; Honkura et al. 2000, 2004; Matsushima et al. 2002; Ujihara et al. 2004; Tang et al. 2010). Based on the numerical examples shown in this paper, we conclude that the numerical computation approach proposed here provides a useful tool for the quantitative studies of seismo-electromagnetic signals. Future case studies of applying the proposed approach can help quantify how much the motional induction effect actually contribute to the coseismic EM signals.

Appendix A: Semi-analytical solutions expressed as wavenumber integrations

According to Eqs. (30) and (31) of Sun et al. (2021) and utilizing recurrence formulas of Bessel function, once the expansion coefficients of seismic displacement $u_{T,m}(z, k)$, $u_{S,m}(z, k)$, and $u_{R,m}(z, k)$ are obtained, the radial, azimuthal, and vertical components of seismic displacement u_r, u_θ, and u_z (i.e., seismic solutions) can be written as

$$u_r(r,\theta,z) = \frac{1}{4\pi}\sum_{m=-\infty}^{+\infty} e^{im\theta}\left\{\int_0^{+\infty}\left[iu_{T,m}(z,k)+u_{S,m}(z,k)\right]J_{m-1}(kr)k\mathrm{d}k + \int_0^{+\infty}\left[iu_{T,m}(z,k)-u_{S,m}(z,k)\right]J_{m+1}(kr)k\mathrm{d}k\right\}, \tag{A1}$$

$$u_\theta(r,\theta,z) = \frac{1}{4\pi}\sum_{m=-\infty}^{+\infty} e^{im\theta}\left\{\int_0^{+\infty}\left[iu_{S,m}(z,k)-u_{T,m}(z,k)\right]J_{m-1}(kr)k\mathrm{d}k + \int_0^{+\infty}\left[iu_{S,m}(z,k)+u_{T,m}(z,k)\right]J_{m+1}(kr)k\mathrm{d}k\right\}, \tag{A2}$$

$$u_z(r,\theta,z) = \frac{1}{2\pi}\sum_{m=-\infty}^{+\infty} e^{im\theta}\int_0^{+\infty}\left[-u_{R,m}(z,k)\right]J_m(kr)k\mathrm{d}k. \tag{A3}$$

Similarly, according to Eqs. (31), (66), and (67) of Sun et al. (2021), EM solutions can be written as

$$\begin{bmatrix} E_r(r,\theta,z) \\ H_r(r,\theta,z)\end{bmatrix} = \frac{1}{4\pi}\sum_{\zeta=SH,PSV}\sum_{p=0,+1,-1}\sum_{m=-\infty}^{+\infty} e^{im\theta}\times \left\{\int_0^{+\infty}\begin{bmatrix} iE^{p,\zeta}_{T,m+p}(z,k)+E^{p,\zeta}_{S,m+p}(z,k) \\ iH^{p,\zeta}_{T,m+p}(z,k)+H^{p,\zeta}_{S,m+p}(z,k)\end{bmatrix}J_{m+p-1}(kr)k\mathrm{d}k + \int_0^{+\infty}\begin{bmatrix} iE^{p,\zeta}_{T,m+p}(z,k)-E^{p,\zeta}_{S,m+p}(z,k) \\ iE^{p,\zeta}_{T,m+p}(z,k)-E^{p,\zeta}_{S,m+p}(z,k)\end{bmatrix}J_{m+p+1}(kr)k\mathrm{d}k\right\}, \tag{A4}$$

$$\begin{bmatrix} E_\theta(r,\theta,z) \\ H_\theta(r,\theta,z)\end{bmatrix} = \frac{1}{4\pi}\sum_{\zeta=SH,PSV}\sum_{p=0,+1,-1}\sum_{m=-\infty}^{+\infty} e^{im\theta}\times \left\{\int_0^{+\infty}\begin{bmatrix} iE^{p,\zeta}_{S,m+p}(z,k)-E^{p,\zeta}_{T,m+p}(z,k) \\ iH^{p,\zeta}_{S,m+p}(z,k)-H^{p,\zeta}_{T,m+p}(z,k)\end{bmatrix}J_{m+p-1}(kr)k\mathrm{d}k + \int_0^{+\infty}\begin{bmatrix} iE^{p,\zeta}_{S,m+p}(z,k)+E^{p,\zeta}_{T,m+p}(z,k) \\ iE^{p,\zeta}_{S,m+p}(z,k)+E^{p,\zeta}_{T,m+p}(z,k)\end{bmatrix}J_{m+p+1}(kr)k\mathrm{d}k\right\}, \tag{A5}$$

$$\begin{bmatrix} E_z(r,\theta,z) \\ H_z(r,\theta,z) \end{bmatrix} = \frac{1}{2\pi} \sum_{\zeta=SH,PSV} \sum_{p=0,+1,-1} \sum_{m=-\infty}^{+\infty} e^{im\theta} \int_0^{+\infty} \begin{bmatrix} -E^{p,\zeta}_{R,m+p}(z,k) \\ -H^{p,\zeta}_{R,m+p}(z,k) \end{bmatrix} J_{m+p}(kr) k \mathrm{d}k. \tag{A6}$$

Obviously, both the seismic and EM solutions, i.e., Eqs. (A1, A2, A3, A4, A5, and A6), are integrations with respect to wavenumber k. The order 'm' in above equations will be limited as $|m| \leq 2$ if a 'source-center' cylindrical coordinate system is chosen to let the point source located in z-axis (Chen 1993, 1999). The above wavenumber integrations can be regarded as summation of several inverse Hankel Transforms, because Bessel function of first kind is contained in every integrand.

Appendix B: Amplitude decay factor of the evanescent EM waves

Evanescent EM waves are generated at an interface when $\theta > \theta_c$ (or $k > \omega/V_{\mathrm{em}}$) which causes γ_{em} $(= \sqrt{k^2 - \omega^2/V_{\mathrm{em}}^2})$ to have a non-zero real part. Following Sun et al. (2021), we can assume the general solutions of the non-localized EM waves (which have EM phase velocity) contain factors like $\exp(\gamma_{\mathrm{em}} z_{\mathrm{rcv}} - i\omega t)$, where $\mathrm{Re}\{\gamma_{\mathrm{em}}\} > 0$ and z_{rcv} represents the depth of an in-air receiver. In this work, we consider the z axis downward positive. Thus, $z_{\mathrm{rcv}} < 0$ and $-z_{\mathrm{rcv}}$ is the normal distance from the in-air receiver to the ground surface ($z = 0$ m). Then, the amplitude decay factor of the evanescent EM waves f_{decay} is determined by

$$f_{\mathrm{decay}}(\omega, z) = \exp(\gamma_{\mathrm{em}} z_{\mathrm{rcv}}). \tag{B1}$$

Considering the relation $k = \sin\theta(\omega/V_{\mathrm{sei}})$, we can obtain

$$\gamma_{\mathrm{em}} = k\sqrt{1 - (V_{\mathrm{sei}} \csc\theta / V_{\mathrm{em}})^2}, \tag{B2}$$

where csc is the cosecant, i.e., $\csc\theta = 1/\sin\theta$. Substituting the above equation into equation (B1) gives

$$f_{\mathrm{decay}}(\omega, z) = \exp\left[k\sqrt{1 - (V_{\mathrm{sei}} \csc\theta / V_{\mathrm{em}})^2} z_{\mathrm{rcv}}\right]. \tag{B3}$$

The EM wave velocity V_{em} is usually much greater than the seismic wave velocity V_{sei}; therefore, the inequation $V_{\mathrm{sei}}\csc\theta/V_{\mathrm{em}} \ll 1$ is usually satisfied unless the seismic incident angle θ is a small value close to zero. Thus, the amplitude decay factor will be determined by

$$f_{\mathrm{decay}}(\omega, z) \approx \exp\left(\omega \frac{\sin\theta}{V_{\mathrm{sei}}} z_{\mathrm{rcv}}\right). \tag{B4}$$

The above equation suggests that the amplitude decay speed of the evanescent EM waves greatly depends on the frequency ω, seismic incident angle θ, and seismic wave velocity V_{sei}.

Abbreviations

EM: Electromagnetic; LAC: Luco–Apsel–Chen; GRT: Generalized reflection and transmission; CGFDM: Curvilinear grid finite-difference method.

Acknowledgements

The authors are grateful to the two anonymous reviewers for their constructive comments and detailed suggestions.

Authors' contributions

LZ, Y-CS and HR carried out the numerical computation. All the authors participated in the discussions of the results. All the authors read and approved the final manuscript.

Funding

This work was jointly supported by the National Natural Science Foundation of China (grant numbers 41974081 and 41874082), Key Special Project for Introduced Talents Team of Southern Marine Science and Engineering Guangdong Laboratory (Guangzhou) (GML2019ZD0203) and Shenzhen Key Laboratory of Deep Offshore Oil and Gas Exploration Technology (grant number ZDSYS20190902093007855). This work was also supported by the Japan Society for the Promotion of Science (JSPS) KAKENHI (grant number JP17K05634).

Availability of data and materials

The velocity structure data of CRUST 1.0 is available from https://igppweb.ucsd.edu/~gabi/crust1.html. The geomagnetic field data of IGRF13 is available from https://www.ngdc.noaa.gov/IAGA/vmod/igrf.html. The numerical computation data are available from Dr. Hengxin Ren (renhx@sustech.edu.cn).

Declarations

Ethics approval and consent to participate

Not applicable.

Consent for publication

Not applicable.

Competing interests

The authors declare that they have no competing interests.

Author details

[1]Shenzhen Key Laboratory of Deep Offshore Oil and Gas Exploration Technology, Southern University of Science and Technology, Shenzhen 518055, Guangdong, China. [2]Department of Earth and Space Sciences, Southern University of Science and Technology, Shenzhen 518055, Guangdong, China. [3]Miyazaki Observatory, Research Center for Earthquake Prediction, Disaster Prevention Research Institute, Kyoto University, 3884, Kaeda, Miyazaki 889-2161, Japan. [4]Department of Geophysics, School of Earth and Space Sciences, Peking University, Beijing 100871, China. [5]Southern Marine Science and Engineering Guangdong Laboratory (Guangzhou), Guangzhou 511458, China.

Received: 23 February 2021 Accepted: 12 June 2021
Published online: 22 June 2021

References

Aki K, Richards PG (1980) Quantitative seismology: theory and methods. W. H. Freeman and Co., London

Alken P, Thébault E, Beggan CD et al (2021) International geomagnetic reference field: the thirteenth generation. Earth Planets Space 73:49. https://doi.org/10.1186/s40623-020-01288-x

Bouchon M (1981) A simple method to calculate Green-functions for elastic layered media. Bull Seismol Soc Am 71(4):957–971

Bouchon M (2003) A review of the discrete wavenumber method. Pure Appl Geophys 160(3):445–465

Bouchon M, Aki K (1977) Discrete wave-number representation of seismic-source wave fields. Bull Seismol Soc Am 67(2):259–277

Chen X (1993) A systematic and efficient method for computing seismic normal modes in layered half-space. Geophys J Int 115:391–409

Chen X (1999) Seismogram synthesis in multi-layered half-space, part I. Theoretical formulations. Earthq Res China 13(2):149–174

Dahlquist G, Björck Å (1974) Numerical methods. Prentice-Hall Inc., Englewood Cliffs, NJ

Dzieran L, Thorwart M, Rabbel W, Ritter O (2019) Quantifying interface responses with seismoelectric spectral ratios. Geophys J Int 217:108–121

Gao Y, Chen X, Hu H, Wen J, Tang J, Fang G (2014) Induced electromagnetic field by seismic waves in Earth's magnetic field. J Geophys Res Solid Earth 119:5615–5685

Gao Y, Wang D, Wen J, Hu H, Chen X, Yao C (2019) Electromagnetic responses to an earthquake source due to the motional induction effect in a 2-D layered model. Geophys J Int 219:563–593

Garambois S, Dietrich M (2002) Full waveform numerical simulations of seismoelectromagnetic wave conversions in fluid-saturated stratified porous media. J Geophys Res 107:40–58

Gershenzon NI, Gokhberg MB, Yunga SL (1993) On the electromagnetic field of an earthquake focus. Phys Earth Planet Inter 77:13–19

Haartsen MW, Pride SR (1997) Electroseismic waves from point sources in layered media. J Geophys Res 102(B11):24745–24769

Honkura Y, Işikara AM, Oshiman N, Ito A, Üçer B, Bariş Ş, Tunçer MK, Matsushima M, Pektaş R, Çelik C, Tank SB, Takahashi F, Nakanshi M, Yoshimura R, Ikeda Y, Komut T (2000) Preliminary results of multidisciplinary observations before, during and after the Kocaeli (Izmit) earthquake in the western part of the North Anatolian Fault Zone. Earth Planets Space 52:293–298. https://doi.org/10.1186/BF03351638

Honkura Y, Satoh H, Ujihara N (2004) Seismic dynamo effects associated with the M7.1 earthquake of 26 May 2003 off Miyagi prefecture and the M6.4 earthquake of 26 July 2003 in northern Miyagi prefecture, NE Japan. Earth Planets Space 56:109–114. https://doi.org/10.1186/BF03353395

Hu H, Gao Y (2011) Electromagnetic field generated by a finite fault due to electrokinetic effect. J Geophys Res 116:B08302

Huang Q, Ren H, Zhang D, Chen JY (2015) Medium effect on the characteristics of the coupled seismic and electromagnetic signals. Proc Jpn Acad Ser B 91(1):17–24

Iyemori T, Kamei T, Tanaka Y, Takeda M, Hashimoto T, Araki T, Okamoto T, Watanabe K, Sumitomo N, Oshiman N (1996) Co-seismic geomagnetic variations observed at the 1995 Hyogoken-Nanbu earthquake. J Geomagn Geoelectr 48(8):1059–1070

Luco JE, Apsel RJ (1983) On the Green's function for a layered halfspace: part I. Bull Seismol Soc Am 73:909–927

Matsushima M, Honkura Y, Oshiman N, Barış Ş, Tunçer MK, Tank SB, Çelik C, Takahashi F, Nakanishi M, Yoshimura R, Pektaş R, Komut T, Tolak E, Ito A, Iio Y, Işıkara AM (2002) Seismoelectromagnetic effect associated with the İzmit earthquake and its aftershocks. Bull Seismol Soc Am 92(1):350–360

Olson AH, Apsel RJ (1982) Finite faults and inverse theory with applications to the 1979 Imperial Valley earthquake. Bull Seismol Soc Am 72:1969–2001

Press F (1964) Seismic wave attenuation in the crust. J Geophys Res 69(20):4417–4418

Pride SR, Moreau F, Gavrilenko P (2004) Mechanical and electrical response due to fluid-pressure equilibration following an earthquake. J Geophys Res 109:B03302

Ren H, Huang Q, Chen X (2007) Numerical simulation of seismoelectromagnetic waves in layered porous media. In: Proceeding of the 8th China international geo-electromagnetic workshop, Jingzhou, Hubei, China, pp 322–329

Ren H, Huang Q, Chen X (2010a) Analytical regularization of the high-frequency instability problem in numerical simulation of seismoelectric wave-fields in multi-layered porous media. Chin J Geophys 53(3):506–511

Ren H, Huang Q, Chen X (2010b) A new numerical technique for simulating the coupled seismic and electromagnetic waves in layered porous media. Earthq Sci 23(2):167–176

Ren H, Chen X, Huang Q (2012) Numerical simulation of coseismic electromagnetic fields associated with seismic waves due to finite faulting in porous media. Geophys J Int 188(3):925–944

Ren H, Huang Q, Chen X (2016a) Numerical simulation of seismo-electromagnetic fields associated with a fault in a porous medium. Geophys J Int 206(1):205–220

Ren H, Huang Q, Chen X (2016b) Existence of evanescent electromagnetic waves resulting from seismoelectric conversion at a solid-porous interface. Geophys J Int 204(1):147–166

Ren H, Huang Q, Chen X (2020) Evanescent EM waves generated by seismoelectric conversion at an interface. In: Grobbe N, Revil A, Zhu Z, Slob E (eds) Seismoelectric exploration: theory, experiments, and applications. Wiley

Sun Y-C, Zhang W, Chen X (2016) Seismic-wave modeling in the presence of surface topography in 2D general anisotropic media by a curvilinear grid finite-difference method. Bull Seismol Soc Am 106(3):1036–1054

Sun Y-C, Zhang W, Chen X (2018) 3D seismic wavefield modeling in generally anisotropic media with a topographic free surface by the curvilinear grid finite-difference method. Bull Seismol Soc Am 108(3A):1287–1301

Sun Y-C, Ren H, Yamazaki K, Zeng L, Huang Q, Chen X (2021) Semi-analytical solutions of seismo-electromagnetic signals arising from the motional induction in 3-D multi-layered media: part I—theoretical formulations. Earth Planets Space 73:20. https://doi.org/10.1186/s40623-020-01327-7

Sun Y-C, Uyeshima M, Ren H, Huang Q, Aizawa K, Tsukamoto K, Kanda W, Seki K, Kishita T, Ohminato T, Watanabe A, Ran J, Chen X (2019) Numerical simulations to explain the coseismic electromagnetic signals: a case study for a M5.4 aftershock of the 2016 Kumamoto earthquake. Earth Planets Space 71:143. https://doi.org/10.1186/BF03351638

Tang J, Zhan Y, Wang LF, Dong ZY, Zhao GZ, Xu JL (2010) Electromagnetic coseismic effect associated with aftershock of Wenchuan Ms 8.0 earthquake. Chin J Geophys 53(3):526–534

Ujihara N, Honkura Y, Ogawa Y (2004) Electric and magnetic field variations arising from the seismic dynamo effect for aftershocks of the M7.0 earthquake of 26 May 2003 off Miyagi Prefecture, NE Japan. Earth Planets Space 56:115–124. https://doi.org/10.1186/BF03353396

Yamazaki K (2012) Estimation of temporal variations in the magnetic field arising from the motional induction that accompanies seismic waves at a large distance from the epicentre. Geophys J Int 190:1393–1403

Zhang W, Chen X (2006) Traction image method for irregular free surface boundaries in finite difference seismic wave simulation. Geophys J Int 167(1):337–353

Zhang HM, Chen X, Chang S (2001) Peak-trough averaging method and its applications to computing synthetic seismograms with shallow focus. Chin J Geophys 44:805–813

Zhang HM, Chen X, Chang S (2003) An efficient method for computing synthetic seismograms for a layered half-space with sources and receivers at close or same depth. Pure Appl Geophys 160:467–486

Zhang W, Zhang Z, Chen X (2012) Three-dimensional elastic wave numerical modelling in the presence of surface topography by a collocated grid finite-difference method on curvilinear grids. Geophys J Int 190(1):358–378

Zhang D, Ren H, Huang Q (2013) Numerical simulation study of co-seismic electromagnetic signals in porous media. Chin J Geophys 56(8):2739–2747

Publisher's Note